# Origin of the moiré pattern in thin Bi films deposited on HOPG

P. J. Kowalczyk*
*The MacDiarmid Institute for Advanced Materials and Nanotechnology, Department of Physics and Astronomy, University of Canterbury, Private Bag 4800, Christchurch 8140, New Zealand and Department of Solid State Physics, Faculty of Physics and Applied Informatics, University of Lodz, 90-236 Lodz, Pomorska 149/153, Poland*

O. Mahapatra, D. Belić, and S. A. Brown
*The MacDiarmid Institute for Advanced Materials and Nanotechnology, Department of Physics and Astronomy, University of Canterbury, Private Bag 4800, Christchurch 8140, New Zealand*

G. Bian and T.-C. Chiang
*Department of Physics, University of Illinois at Urbana-Champaign, 1110 West Green Street, Urbana, Illinois 61801-3080, USA*
(Received 23 October 2014; published 28 January 2015)

Thin Bi(110) films deposited on highly oriented pyrolytic graphite (HOPG) exhibit a pronounced moiré pattern; here the origin of the moiré pattern is investigated using scanning tunneling microscopy (STM) and spectroscopy (STS), high-resolution transmission electron microscopy (HR-TEM), and density functional theory (DFT). It is shown that the moiré pattern forms only on islands which are misoriented by $\sim 30^{\circ}$ with respect to the usual substrate symmetry direction. Two models of the moiré pattern are presented: (i) a commensurate monolayer construction (CMC) for rectangular overlayer symmetry on hexagonal substrates and (ii) a qualitative model based on simple superposition of a Bi overlayer on graphene. The CMC model has previously been applied only to systems with pure hexagonal symmetry. Both models generate moiré patterns with key parameters (period, angles of the pattern measured with respect to the main HOPG and Bi crystal directions) that are consistent with the experimental results, but development of a fully predictive/quantitative model remains an outstanding challenge. The electronic structure of the moiré pattern is investigated using STS and DFT, and it is found that the local density of states (LDOS) is modulated by the moiré pattern. These results are consistent with a picture in which a small distortion of Bi atomic positions at the film-substrate interface results in periodic modulation of the LDOS, hence allowing observation of the moiré pattern in STM images.

DOI: 10.1103/PhysRevB.91.045434 PACS number(s): 81.05.Bx, 68.55.−a, 73.90.+f, 61.44.Fw

## I. INTRODUCTION

The formation of moiré patterns in incommensurate layered structures has been the subject of much interest for over two decades [1–27] and has been investigated using transmission electron microscopy (TEM) [3–5], low-energy electron diffraction (LEED) [7,8], and scanning tunneling microscopy (STM) [5,5–27]. A significant application of these patterns is in nanotechnology as substrates for ordered growth of metallic clusters and self-assembly of atoms [21,22], but (as we show below) moiré patterns could also have a significant impact on the topological properties [28,29] of some materials. We are particularly interested in bismuth [30] and its alloys [31,32], which have strong spin-orbit coupling and novel electronic properties.

Moiré patterns were previously observed for nanostructured bismuth films deposited on GaAs [15], Au [33], Si(111) [34], and quasicrystals [35]; however, no detailed investigation of the origin of these patterns was performed until now. We show here that moiré patterns are observed for 3 monolayer (ML) thick Bi islands on highly oriented pyrolytic graphite (HOPG) and investigate the morphological and electronic structure of these islands using STM and scanning tunneling spectroscopy (STS).

The moiré pattern is present in only ∼20% of islands which have an unusual orientation with respect to the substrate [Bi $\langle \bar{1}10 \rangle$ aligned with the HOPG armchair ($\langle 10\bar{1}0 \rangle$) direction, instead of the more usual HOPG zigzag ($\langle 1\bar{1}00 \rangle$) direction [36]]. This is clearly seen in islands with a tilt grain boundary (GB) [37] in which the moiré pattern is observed only in one grain. We show that these experimental results are consistent with results of simulations performed using two methods: a commensurate monolayer construction (CMC) [38] and a simple superposition model.

Our analysis suggests that the observed moiré pattern is not related to morphological deformation of the surface. Instead, the moiré pattern manifests itself as a modulation of the local density of states (LDOS), which itself results from displacement of Bi atoms at the interface with the substrate. Our density functional theory (DFT) calculations show that such deformation locally changes the electronic structure of the material, and we believe that this allows the moiré pattern to be observed through STM measurements.

For Bi thin films the observation of moiré patterns leads to many interesting possibilities because of the strong spin-orbit (SO) coupling in Bi [39,40]. For very thin films the electronic states on the two surfaces are degenerate, so the effects of SO splitting are usually lost [30,41]. However, for distorted films we show the degeneracy is lifted, and as a consequence, periodic deformation at the film-substrate interface could generate periodic spin texture commensurate with the moiré

*pkowa@uni.lodz.pl

 

pattern. This opens up new possibilities in the fields of topological insulators [28,29,31,32] and spintronics [42].

### A. Bismuth and film morphology

Bismuth is a semimetal characterized by a low concentration of charge carriers [39,43], small and anisotropic effective masses [39,44], de Broglie wavelengths up to 40 nm [45], and mean free paths up to 100 nm at room temperature (and 400 $\mu$m at 4.2 K) [45]. Its surface is more metallic than the bulk due to formation of spin-orbit split surface states [39,43,46]. Because of these properties, the surfaces of Bi structures are promising candidates for the observation of quantum effects, particularly in structures with reduced dimensionality. For example, superconductivity manifests itself in small Bi clusters [47], quantum size effects drive (i) lateral growth [30], (ii) shifts of the Fermi level [48], and (iii) semimetal to semiconductor transitions [49,50], and topological Hall states have been predicted [51] and observed experimentally [52].

We focus here on bismuth films deposited on HOPG. This system is well characterized [30,36,37,53–57] and consists of 0.98-nm-thick (3-ML-thick) bases on top of which successive 0.66-nm (2-ML) stripes grow, forming the sequence 3, 5, 7 ML with the (110) plane (using rhombohedral indices) parallel to the substrate (see Fig. 1). The elongation direction of the islands (stripes and rods) is Bi$\langle\bar{1}10\rangle$, which is usually found to be parallel to HOPG zigzags ($\langle 1\bar{1}00\rangle$) [36]. The majority of islands are rotated by 60° with respect to one another due to hexagonal symmetry of the substrate [36,54,55] and the fact that Bi rods that are oriented at 0° with respect to any particular substrate symmetry direction are indistinguishable from those that are rotated by 180°.

The observation of paired layer growth of Bi on a variety of substrates [56,58–60] is consistent with the formation

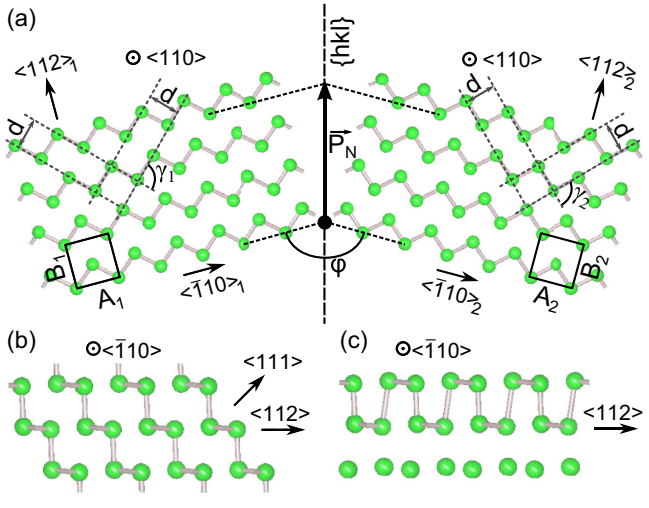


FIG. 1. (Color online) Bi(110) crystallographic structure and model grain boundary. (a) Intersection of two grains at a tilt grain boundary showing the unit cell dimensions $A, B$, interrow spacing $d$, and key crystallographic directions in each grain. See Appendix A for details of the description of the grain boundary. Cross-section views (along the $\langle\bar{1}10\rangle$ direction) for (b) bulk-like and (c) black-phosphorus-like structures.

of a black-phosphorous-like (BP) thin-film allotrope [see Fig. 1(c)] [59]. However, the structure of thin films is still uncertain because arguments both for and against the BP-like allotrope exist [30,56,57,60]. Fortunately, the surface unit cell of allotropic thin films is almost identical to that of films with the bulk structure, so this ambiguity is not important for the present analysis. The role of a wetting layer, which in the case of Bi on HOPG is always hidden under the islands, is also still uncertain, but it appears to have no measurable influence on the electronic properties of the islands [30].

#### *Unit cell and unit vectors*

The unit vectors for Bi(110) are shown in Fig. 1(a) and are defined as

$$\vec{A} = \vec{a}_2 - \vec{a}_1 = (a,0,0), \quad \vec{B} = \vec{a}_3 = (0,\sqrt{3}a/3,c/3), \qquad (1)$$

where $\vec{a}_1, \vec{a}_2, \vec{a}_3$ are the basis vectors as defined in Ref. [39] and $a^{\text{bulk}} = 0.454$ nm and $c^{\text{bulk}} = 1.179$ nm. These parameters can be expressed using the rhombohedral lattice constant $a_{rh}^{\text{bulk}} = 0.475$ nm and the angle between unit vectors $\alpha^{\text{bulk}} = 57.35°$:

$$a = a_{rh}\sqrt{2[1-\cos(\alpha)]}, \quad c = a_{rh}\sqrt{3[1+2\cos(\alpha)]}, \qquad (2)$$

which results in the surface unit cell for Bi(110): $A \times B = 0.454 \times 0.475$ nm$^2$. The surface unit cell contains two atoms, one at the origin and the other slightly off center [see Fig. 1(a)]. For convenience, we define

$$\beta = \sqrt{2[1-\cos(\alpha)]}, \qquad (3)$$

so that $A = \beta a_{rh}$ and $B = a_{rh}$.

### B. Moiré patterns

Most of the early STM work interpreted moiré patterns as resulting from tip effects [13,14] or misorientation of substrate layers [14–18]. It was Kobayashi [5,6] who first explained that moiré patterns could arise from modulation of the electronic states in an overlayer due to the interaction with a substrate.

STS experiments [8–12] confirmed Kobayashi's prediction [5] of the dependence of STM images on bias voltage and hence the importance of electronic effects. It is important to understand that the moiré effect can therefore be observed in STM even in the absence of a modulation of the surface height, which is consistent with the lack of observations of moiré patterns using atomic force microscopy (AFM) [5] [AFM is less sensitive to the electronic structure of the material [61]; moiré patterns are expected to be observed by AFM only if a real (vertical) modulation of the surface is present [27]].

The absence of *surface* deformation does not necessarily indicate that the *film-substrate* interface is also deformation free: deformation at the interface between a Si substrate and Pb islands results in observation of the Si(111) $7 \times 7$ reconstruction in STM images of the surface of Pb islands [62]; similarly, subsurface deformations associated with moiré patterns are manifested in STM images in Refs. [11,12]. In this work we show that similar effects are responsible for the observation by STM of moiré patterns in Bi islands grown on HOPG.

The approach to a detailed understanding of the origin of moiré patterns proposed by Kobayashi [5,6] is ideal but

requires calculations of the electronic states of a complex system comprising the overlayer and substrate atoms and taking into account interactions between them. Such calculations are very often difficult to perform due to the large unit cells (and huge number of atoms) involved, as well uncertainties in the details of the atomic positions at the interface and the correct interaction potentials. These issues are especially relevant in the present work, where (see below) the moiré patterns have large periods and the band structure of the Bi overlayer is particularly sensitive to small atomic displacements. Thus, we consider two simpler approaches to modeling the patterns that result from the superposition of the substrate and the overlayer in order to explain the periodicity and rotation angle of the moiré patterns observed with STM. Although the geometry was different, a similar approach was previously taken to explain the moiré pattern observed for Pb on Si(111) [63].

#### *Characterization of the moiré pattern*

In our STM and TEM experiments we focus on characterizing the moiré pattern by measurement of (i) $\lambda$, the periodicity of the moiré pattern, and (ii) $\delta$, the angle between the stripes that form the moiré pattern and Bi$\langle\bar{1}10\rangle$ (the direction along which the Bi islands are elongated [36]), which depend on the orientation of the islands with respect to the substrate, i.e., on (iii) $\theta$, the angle between the Bi$\langle\bar{1}10\rangle$ and HOPG $\langle10\bar{1}0\rangle$ directions.

## II. EXPERIMENT

Commercially available HOPG (SPI-1) was used as a substrate in all experiments. It was cleaved in air, then loaded into the UHV system and annealed at 700–900 K for 16 h to remove contaminants. After the substrate cooled down to room temperature, high-purity bismuth (99.999%) was evaporated from a ceramic crucible and deposited onto the substrate at rates of ∼0.01 Å/s. The film thickness was monitored with a calibrated quartz crystal and was measured in units of monolayers. Here we define 1 ML as the thickness equivalent to that of a single rhombohedral Bi(110) plane, i.e., 3.3 Å [53].

STM measurements were carried out using an Omicron UHV STM at a base pressure of $10^{-8}$ Pa at 50 K (LT) and room temperature (300 K), using cut Pt90%-Ir10% tips. Typical scanning parameters used during measurements were $V_{\text{bias}} = -0.8$ V and $I = 10$ pA. STS measurements (±1.0 V, 128 points per curve) were done in current imaging tunneling spectroscopy mode (CITS, 128 × 128 points$^2$). All STS/CITS measurements were done at LT. $dI/dV$ was calculated numerically.

Samples for HR-TEM measurements were grown on peeled-off flakes of HOPG mounted on gold TEM grids. After the growth samples were vented using $N_2$ gas and transferred in $N_2$ atmosphere to a Philips CM200 HR-TEM; they were exposed to air during the holder exchange and loading procedure for less than 2 min (dose $\lesssim 10^{12}$ L). This transfer technique does not significantly affect the morphology of the islands, and the small number of lifted-off graphite layers ($\leqslant$20) allows excellent imaging.

First-principles calculations [64] of the electronic structure of the films were performed using Hartwigsen-Goedecker-Hutter-type pseudopotentials and a plane-wave basis set. The main program employed was developed by the ABINIT group. Spin-orbit coupling was included using the relativistic local-density approximation. Densities of states are calculated by integrating over the entire Brillouin zone. The surfaces were relaxed for all film thicknesses, resulting in subtle but important differences in atomic arrangement compared to those in Ref. [65].

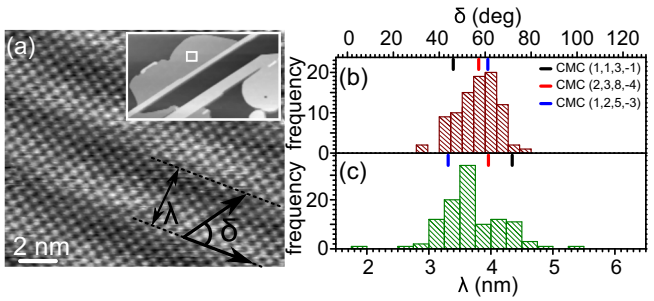


FIG. 2. (Color online) (a) High-resolution STM image ($V = -2$ V, $I = 1.5$ nA) recorded at 300 K clearly showing the moiré pattern ($\lambda = 4.0$ nm) recorded in the rectangular region of the low-resolution image in the inset. (b) Distribution of measured moiré angles $\delta$. (c) Distribution of measured moiré periodicities $\lambda$. Black, red, and blue markers in (b) and (c) correspond to $\delta$ and $\lambda$ obtained from the CMC model for three sets of indices $(n,m,u,v)$; see text.

## III. RESULTS

### A. STM results

#### *1. Islands without grain boundaries*

Our STM investigations allow us to image the Bi islands and rods grown on the HOPG substrates and to routinely observe atomic corrugations [30,56,57]. Occasionally, we also observe an additional long-wavelength periodicity which we identify as a moiré pattern. An example of such additional periodicity is shown in Fig. 2(a). The moiré pattern was observed only in about 20% of the 3-ML-thick islands (80% are featureless). No moiré pattern was observed in STM images of islands thicker than 3 ML. The pattern shown in Fig. 2(a) can be characterized by $\lambda = 4 \pm 1$ nm and $\delta = 56^\circ \pm 3^\circ$. We have measured $\lambda$ and $\delta$ for moiré patterns observed on several dozen different islands, as shown in Figs. 2(b) and 2(c): $\delta$ is in the range 40° to 70°, and $\lambda$ is in the range 3 to 4.5 nm.

#### *2. Islands with grain boundaries*

Figure 3(a) shows an STM image of a large island with a 3-ML base on top of which are stripes which meet at an angle of ∼90°. This indicates the presence of a grain boundary. Grain boundaries in this system were discussed extensively in Ref. [37], so in Appendix A we repeat only the most important details. Figure 3(a) shows the most common [37] tilt grain boundary $\Sigma 1$ [see Fig. 3(c) for ball model] separating grains denoted 1 and 2 in Fig. 3(a). The measured dihedral angle between the grains is $\varphi = 94^\circ \pm 2^\circ$. Our STM images suggest that the unit cells vary between grains: in Fig. 3(a) the unit cells are $(0.44 \pm 0.02 \times 0.48 \pm 0.02)$ nm$^2$ and $(0.46 \pm 0.02 \times 0.48 \pm 0.02)$ nm$^2$ for grains 1 and 2, respectively.

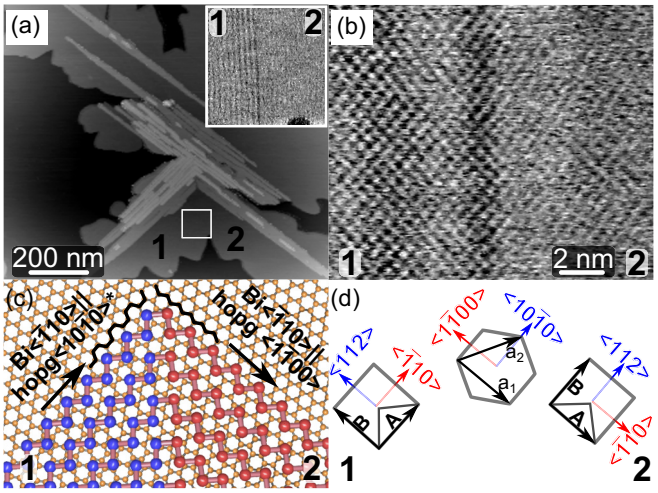


FIG. 3. (Color online) (a) STM image ($V = -0.8$ V, $I = 10$ pA) of a 3-ML-thick Bi island recorded at 50 K showing two grains (labeled 1 and 2) separated by a $\Sigma 1$ tilt grain boundary. The inset in (a) shows a fast Fourier transformation enhanced STM image ($V = -0.3$ V, $I = 10$ pA) of the rectangular region marked in the main plot, showing that the moiré pattern ($\lambda = 4.4$ nm) is observed only in grain 1. (b) Magnification of the central part of the inset showing atomic resolution ($V = -0.3$ V, $I = 0.5$ nA). Unit cells in grains 1 and 2 are $0.44 \times 0.48$ and $0.46 \times 0.48$ nm$^2$, respectively. (c) Model of $\Sigma 1$ tilt grain boundary. Bi$\langle \bar{1}10 \rangle$ is nearly parallel to the HOPG armchair ($\langle 10\bar{1}0 \rangle$) direction in grain 1 and is parallel to the HOPG zigzag ($\langle 1\bar{1}00 \rangle$) direction in grain 2. Armchairs and zigzags for HOPG are indicated using thick lines in (c). (d) Left: Bi surface unit cell for grain 1, center: HOPG unit cell, and right: Bi surface unit cell for grain 2, showing the main crystallographic directions.

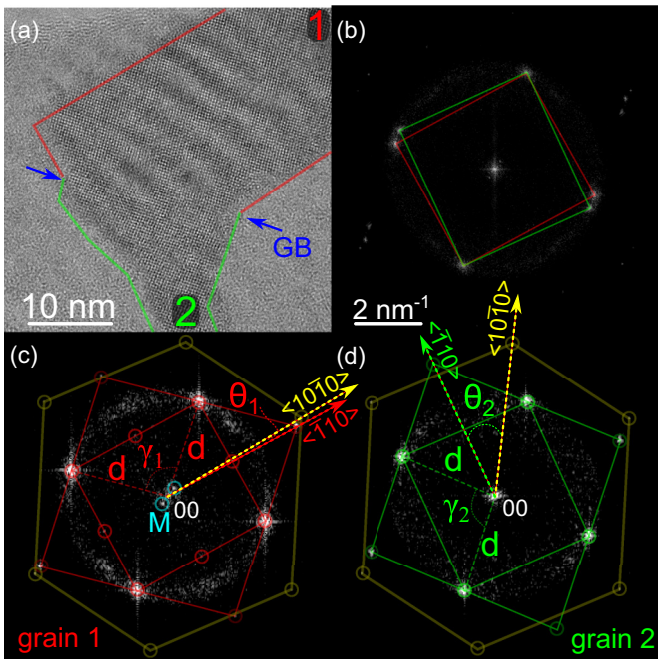


FIG. 4. (Color online) (a) HR-TEM image recorded on an island with a $\Sigma 1$ tilt grain boundary (marked with blue arrows). Grains 1 and 2 are bordered using red and green lines, respectively. The image was enhanced using FFT filtering in order to more clearly show the moiré pattern in grain 1. (b) FFT of the image in (a). Reciprocal unit cells for grains 1 (red) and 2 (green) are shown. FFTs calculated for (c) grain 1 and (d) grain 2 individually. Clear moiré spots (marked M) are seen in (c), corresponding to $\lambda \sim 3.5$ nm. Crystallographic directions of Bi$\langle \bar{1}10 \rangle$, HOPG$\langle 10\bar{1}0 \rangle$, and $\theta$, $d$, $\gamma$ are shown in (c) and (d).

Closer inspection of the image shown in Fig. 3(b) allows one to identify a moiré pattern in grain 1. This pattern is much clearer in the inset in Fig. 3(a): the stripes in the pattern are equally separated ($\lambda \sim 4$ nm, with $\delta \sim 47°$) and are oriented parallel to the grain boundary. The existence of the moiré pattern in only one grain suggests that its origin is related to misorientation of the Bi film with respect to the substrate. The Bi$\langle \bar{1}10 \rangle$ direction is parallel to the HOPG zigzag direction ($\langle 1\bar{1}00 \rangle$) in grain 2 and is nearly parallel to the HOPG armchair direction (i.e., $\langle 10\bar{1}0 \rangle$) in grain 1 [see Fig. 3(c) for ball model and crystallographic directions]. Knowledge of the dihedral angle $\varphi = 94° \pm 2°$ allows one to estimate $\theta = 4° \pm 2°$ for grain 1 ($\theta = \varphi - 90°$; see Appendix A), while $\theta \sim 30°$ for grain 2.

### B. HR-TEM results

Moiré patterns can also be observed in HR-TEM images; an example is shown in Fig. 4(a) for a 5-ML-thick island with a $\Sigma 1$ tilt grain boundary (see Ref. [37] and Appendix A). We were never able to obtain clear images of 3-ML-thick islands in HR-TEM images because they are simply too thin.

A fast Fourier transform (FFT) of the image obtained for grain 1 [see Fig. 4(c)] shows spots identified with the Bi and HOPG lattices but also reveals an additional pair of spots denoted M. These spots are absent in the FFT image obtained for grain 2 [Fig. 4(d)]. The position of the spots allows estimates for grain 1 of $\lambda = 3.5 \pm 0.5$ nm and $\delta \sim 35° \pm 5°$, which are at low end of the range of values estimated by STM (see Fig. 2).

At first sight, the crystallographic structure of both grains in Fig. 4(a) is the same. However, the more detailed analysis performed using FFT shown in Figs. 4(b)–4(d) allows some subtle changes of the interatomic distances between grains to be seen. Close inspection of Figs. 4(c) and 4(d) reveals that the $\gamma_1$ and $\gamma_2$ angles [see Fig. 1(a)] are different and equal to $93° \pm 1°$ and $91° \pm 1°$, respectively. At the same time the interplane distance $d$ [see Figs. 4(c) and 4(d)] is the same for both grains and is equal to $0.33 \pm 0.01$ nm. Knowledge of $d$ and $\gamma$ allows an estimate of the Bi(110) unit cell dimensions using Eq. (A4): $A \times B = 0.45 \times 0.49$ and $0.46 \times 0.47$ nm$^2$ for grains 1 and 2, respectively (uncertainties of 0.01 nm), in very good agreement with STM results.

The series of outer spots in the FFT images [marked yellow in Figs. 4(c) and 4(d)] correspond to graphite (the thin layers peeled off the substrate could be thought of as multilayer graphene), so it is clear that the Bi$\langle \bar{1}10 \rangle$ direction for grain 1 is nearly parallel to HOPG$\langle 10\bar{1}0 \rangle$ [see Fig. 4(c) with $\theta_1 = (2 \pm 1)°$]. In contrast, Bi$\langle \bar{1}10 \rangle$ for grain 2 is nearly parallel to direction of the zigzags on the substrate ($\theta_2 = 35° \pm 1°$). These values of $\theta$ are in good agreement with our STM estimates in the previous section, and again the moiré pattern is observed only when Bi$\langle \bar{1}10 \rangle$ is nearly parallel to HOPG$\langle 10\bar{1}0 \rangle$.

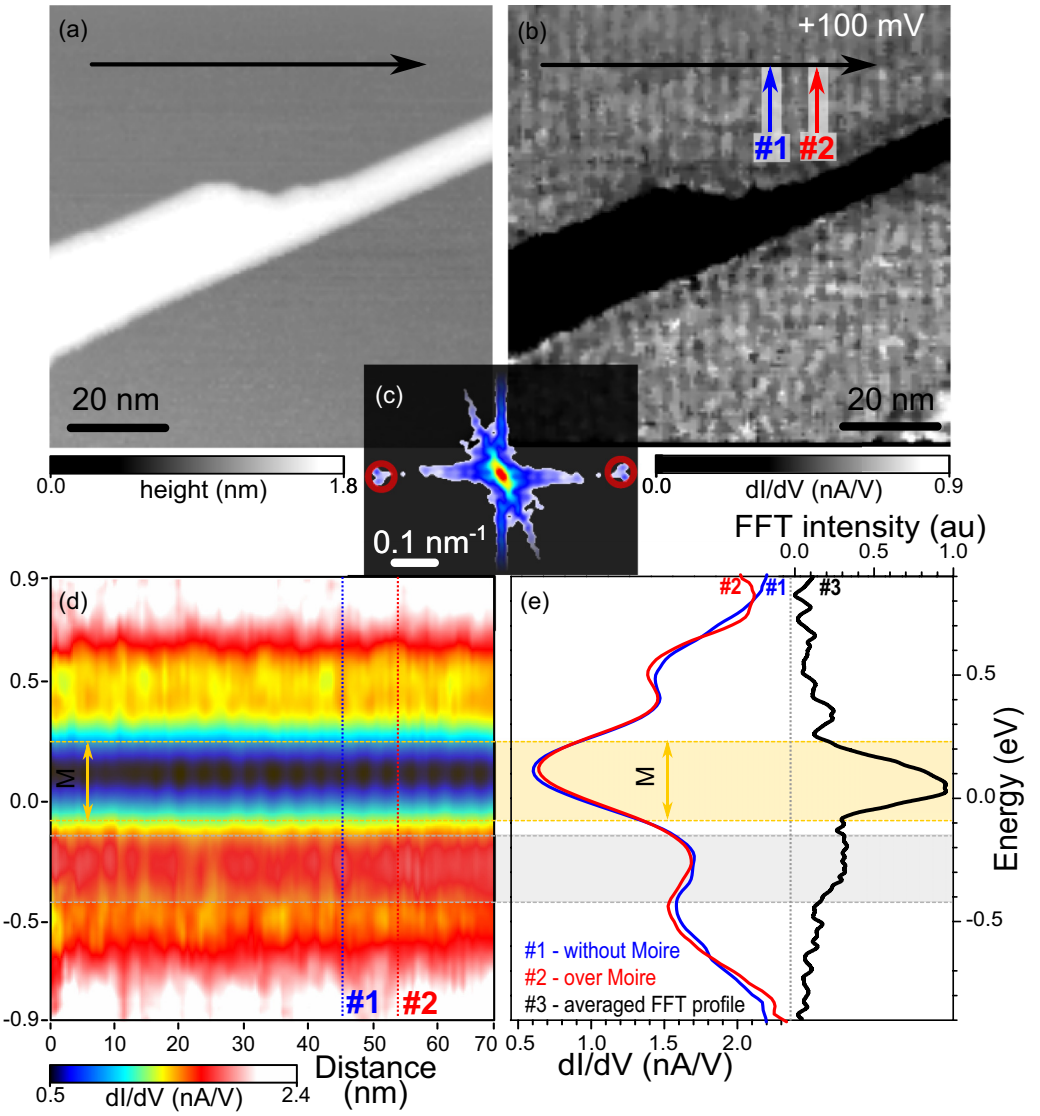


FIG. 5. (Color online) (a) STM image ($V = 1.0$ V, $I = 1.0$ nA) showing a 3-ML-thick region with a 5-ML stripe. (b) $dI/dV$ image for $V = +100$ mV corresponding to the topographic image in (a), revealing the moiré pattern in the 3-ML region. (c) FFT power spectrum calculated for (b). Red circles indicates spots corresponding to the moiré pattern in (b). (d) Tunneling conductance map recorded along the line shown in (a) and (b). (e) Two tunneling conductance curves recorded on moiré intensity minimum and moiré intensity maximum as indicated by arrows 1 and 2 in (b). These positions are also indicated using vertical lines in (d). Line 3 is the normalized FFT intensities (see Appendix B) as a function of the energy recorded for moiré pattern [red circles in (c)].

### C. STS results: Bias voltage dependence of the moiré pattern

In this section we describe STS measurements, which provide a probe of the electronic states in the Bi films. Figure 5(a) shows an STM topography image of a 5-ML stripe separating two 3-ML-high regions. The moiré pattern is barely seen in the topographic image (recorded for a bias voltage of 1 V). Its presence in the 3-ML-high regions is, however, clear in the corresponding $dI/dV$ image recorded at 100 mV [Fig. 5(b)] and the FFT of that image shown in Fig. 5(c). Since the $dI/dV$ signal is proportional to the LDOS in the film, these data are strong evidence for a modulation of the Bi electronic states associated with the moiré pattern.

Further insight into this modulation can be gained from the $dI/dV$ line profile [recorded along the line indicated in Figs. 5(a) and 5(b)] and two representative $dI/dV$ curves shown in Fig. 5(e) [curves are recorded in positions 1 and 2, indicated by arrows and lines in Figs. 5(b) and 5(d), respectively]. The overall shape of the $dI/dV$ curves [Fig. 5(e)] is characterized by two maxima located at $-0.2$ and $+0.4$ eV and a deep valley centered $\sim$0.1 eV above the Fermi level. The $dI/dV$ line profile [Fig. 5(d)] reveals a periodic modulation of the LDOS in the valley region [denoted M in Figs. 5(d) and 5(e)].

Further inspection of the $dI/dV$ line profile and curves 1 and 2 in Fig. 5(e) reveals that some peaks in the LDOS are modulated in antiphase to the modulation of the LDOS valley; for example, whenever the LDOS for region M increases, the LDOS decreases at $-0.2$ eV and vice versa. The modulation of the peak at $-0.2$ eV is much weaker than the modulation of the M feature, so, as described in Appendix B, we developed a technique based on analysis of the FFT images to demonstrate

it more clearly [see curve 3 in Fig. 5(e), which shows a modulation across a broad range of energies].

## IV. MODELS OF THE MOIRÉ PATTERN

Our STM and HR-TEM measurements show that the moiré pattern is observed only for grains with Bi$\langle\bar{1}10\rangle$ approximately parallel to HOPG$\langle 10\bar{1}0\rangle$. This observation allows us to explore two different possible models of the moiré pattern (quantitative and qualitative) based on rotations of the Bi overlayers with respect to the HOPG substrate.

### A. Quantitative model: Commensurate monolayer construction

In order to identify all possible commensurate structures we use the so-called commensurate monolayer construction method proposed by Tkatchenko [38]. The CMC method was previously used for overlayers with hexagonal symmetry on (111) surfaces and, for example, was successfully used to explain the origin of the moiré structure in $C_{60}$ on Pb [66]. Bi(110) is not hexagonal, so we present here a CMC model for rectangular overlayer symmetry on hexagonal substrates.

The CMC problem is defined by

$$n\mathbf{R}\vec{A} + m\mathbf{R}\vec{B} = u\vec{a_1} + v\vec{a_2}, \tag{4}$$

where $n$, $m$, $u$, $v$ are integers and $\mathbf{R}$ is a $2\times 2$ rotation matrix through angle $\theta$. The lattice vectors for HOPG are $\vec{a_1} = d_G(\sqrt{3}/2, 1/2)$, $\vec{a_2} = d_G(\sqrt{3}/2, -1/2)$, where $d_G = 0.244$ nm is the length of HOPG lattice vector. For bismuth $\vec{A} = \beta a_{rh}(1,0)$, $\vec{B} = a_{rh}(0,1)$, as in Sec. I A. Each set of indices $(n,m,u,v)$ represents a different solution of Eq. (4), i.e., a different commensurate structure which is characterized by different value of $\theta$ and a different Bi unit cell (defined by $a_{rh}$ and $\alpha$). If both the Bi and HOPG unit cells were fixed, there would be a limited number of solutions of the model, but here the situation is complicated by the apparent variation of the Bi unit cell in experiments, and we must allow $a_{rh}$ to vary; we do this by varying $\alpha$. Equation (4) can be solved and $a_{rh}$, $\theta$ and $\delta$ can be extracted as a function of $n$, $m$, $u$, $v$, and $\alpha$:

$$a_{rh}(n,m,u,v,\alpha) = \frac{d_G\sqrt{3}/2(u+v)}{\beta n\cos(\theta) - m\sin(\theta)}, \tag{5}$$

$$\theta(n,m,u,v,\alpha) = \arctan\left(\frac{\beta n(u-v) - \sqrt{3}m(u+v)}{m(u-v) + \sqrt{3}\beta n(u+v)}\right), \tag{6}$$

$$\delta(n,m,u,v,\alpha) = \arccos\left(\frac{(u+v)}{\sqrt{(u+v)^2 + (u-v)^2/3}}\right) - \theta, \tag{7}$$

where $\beta$ is a function of $\alpha$ [see Eq. (3)].

The results for $(n,m,u,v) \in (-50,50)$ and $\alpha^{\text{bulk}} = 57.3^\circ$ are shown in Fig. 6(a). Similar results for smaller $\alpha$ ($54.8^\circ$) are shown in Fig. 6(b). Experimentally reasonable values of

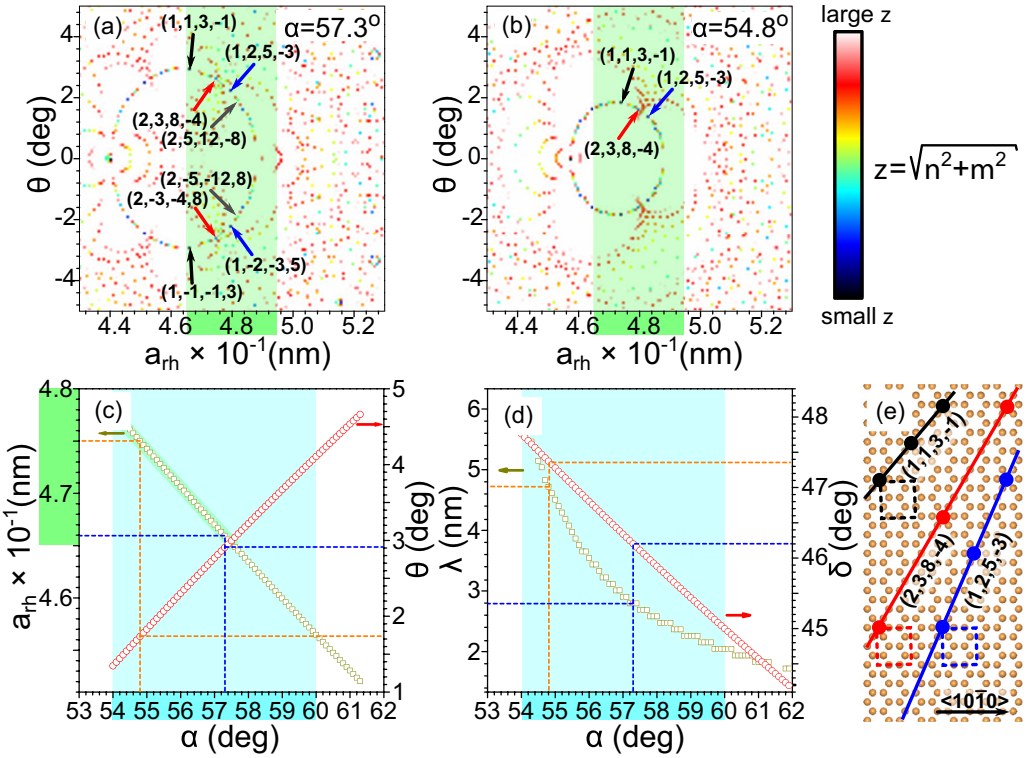


FIG. 6. (Color online) Results of calculations using commensurate monolayer construction. (a) Solutions $(a_{rh}, \theta)$ of Eqs. (5) and (6) for $\alpha = 57.3^\circ$. (b) Solutions for $\alpha = 54.8^\circ$. The color scale is an indication of the distance between adjacent commensurate sites, $z = \sqrt{n^2+m^2} < 10$. Arrows highlight indices $(n,m,u,v)$ discussed in the text. (c) Dependence of $a_{rh}$ and $\theta$ on $\alpha$ for $(n,m,u,v) = (1,1,3,-1)$. (d) Dependence of $\lambda$ and $\delta$ on $\alpha$ for $(1,1,3,-1)$. Dashed lines indicate $a_{rh}$, $\theta$, $\lambda$, and $\delta$ for $\alpha = 54.8^\circ$ and $\alpha = 57.3^\circ$. (e) Ball model showing commensurate sites for three sets of indices, $(n,m,u,v)$. Lines show the direction of moiré stripes with respect to the underlying HOPG. The surface unit cells are indicated using dashed lines. Green and cyan shadings in (a)–(d) indicate the maximal ranges of $a_{rh}$ and $\alpha$ that could be consistent with experiment.

$a_{rh}$ are indicated by green shading. Each plotted point (i.e., $a_{rh}$, $\theta$ pair) corresponds to a possible commensurate structure represented by indices $(n,m,u,v)$. The color scale in these plots corresponds to the minimum distance $z = \sqrt{n^2 + m^2}$ between bismuth atoms that are commensurate with hollows in the uppermost substrate layer. We focus on $z \leqslant 10$ (blue and black points) as a way of highlighting the simplest solutions, with the smallest possible indices $(n,m,u,v)$.

#### 1. Solution with the smallest indices

The solution with the smallest possible indices is $(n,m,u,v) = (1,1,3,-1)$. Figure 7 shows ball models of the moiré pattern for that set of indices and for $(1,-1,-1,3)$, which generates a mirror-image pattern (here $\alpha^{\text{bulk}} = 57.3°$; hence $a_{rh} = 0.466$ nm [from Eq. (5)] and $\theta = +2.9°, -2.9°$ [from Eq. (6)]). Atoms located in HOPG hollow sites are colored green. These commensurate atoms are arranged along line A in Fig. 7(a).

A key aspect of the CMC model is that Bi atoms are perfectly commensurate with substrate hollow sites only along line A and *not* in the perpendicular direction. $\lambda$ is not determined in a simple way by the solutions of Eqs. (5)–(7). Figure 7(a) shows that there are other *nearly* commensurate lines (denoted B, C, D). The Bi atoms in line B are shifted with respect to the underlying HOPG hollow sites by $<1\%$

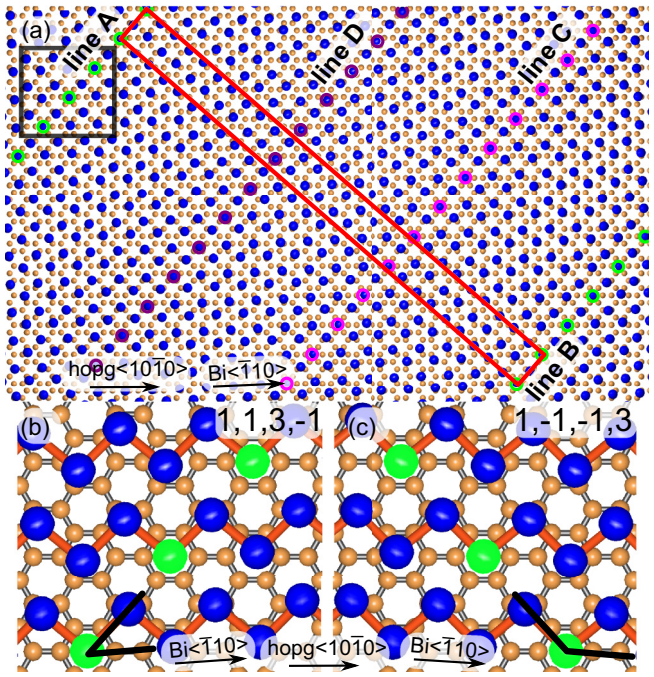


FIG. 7. (Color online) CMC model. (a) Ball model for $(n,m,u,v) = (1,1,3,-1)$ ($\alpha = 57.3°$, $a_{rh} = 0.466$ nm, and $\theta = +2.9°$). Green atoms in line A are in perfect commensuration with the centers of HOPG hollow sites. Atoms in lines B and C are *nearly* commensurate with hollow sites of HOPG; for example, green atoms in line B are shifted with respect to underlying HOPG hollow sites by $<1\%$. The red rectangle shows the moiré pattern unit cell defined by two vectors, (1,1) and (14, −13). (b) The region indicated using a black rectangle in (a), shown in more detail. (c) Ball model for $(n,m,u,v) = (1,-1,-1,3)$ with $\theta = -2.9°$. Acute and obtuse $\delta$ angles are highlighted in (b) and (c).

in comparison to the Bi atoms in line A, but they are *not* perfectly commensurate. Therefore, the periodicity in the direction perpendicular to line A is affected by the tolerance with which one defines "commensuration." The situation is further complicated by lines C and D, which are sites at which atoms *in the center* of the Bi unit cell (see Fig. 1) are nearly commensurate with the HOPG hollow sites (the commensuration is high for line C and lower for D). Thus, in this particular example, the moiré pattern includes three parallel lines of commensurate atoms with different levels of commensuration. The unit cell for this moiré pattern is shown in Fig. 7(a) and is created by two $(n,m)$ vectors: (1,1) and (14, −13). While the simulations allow calculation of $\delta$ from Eq. (7), there is no obvious algorithm that would allow determination of $\lambda$, which can be found only by manual inspection.

#### 2. Range of moiré periodicity and orientations for $(n,m,u,v) = (1,1,3,-1)$

For a single set of indices $(n,m,u,v)$ it is possible to analyze the dependence of $\theta$, $\lambda$, and $\delta$ on $\alpha$. Plots for $(n,m,u,v) = (1,1,3,-1)$ are shown in Figs. 6(c) and 6(d). The estimate of $\lambda$ assumes a tolerance of $<8\%$ for misalignment of Bi atoms (in lines B, C, D) with respect to the substrate hollow sites. Figures 6(c) and 6(d) show that an increase of $\alpha$ results in (i) a reduction of $a_{rh}$, (ii) an increase of $\theta$, (iii) a reduction of $\lambda$, and (iv) a reduction of $\delta$.

Some of the $\theta$, $\lambda$, $\delta$ values which can be read from Fig. 6 are in relatively good agreement with our experimental results while others are not. In particular for $\alpha^{\text{bulk}} = 57.3°$ [$A \times B = 0.447 \times 0.466$ nm$^2$ from Eq. (5)] one obtains $\theta = 2.9°$, $\delta = 46.2°$, and $\lambda = 2.8$ nm [see blue dashed lines in Figs. 6(c) and 6(d)]. This value of $\lambda$ is at the lower end of the range of experimental values. If we reduce $\alpha$, we find that $\delta$ and $\lambda$ both increase; for example, for $\alpha = 54.8°$ [corresponding to $A \times B = 0.437 \times 0.475$ nm$^2$, from Eq. (5)] $\theta = 1.7°$, $\delta = 47.3°$, and $\lambda = 4.7$ nm [orange dashed lines in Figs. 6(c) and 6(d)], which are all in reasonable agreement with the experimental results [see black bar in Figs. 2(b) and 2(c)]. Note, however, that using the set of indices (1,1,3, −1) alone it is not possible to reproduce the range of experimentally observed $\delta$ angles [40°–80°; Fig. 2(b)]: for (1,1,3, −1), $\delta$ is limited to 44°–48° for reasonable values of $\alpha$ and $a_{rh}$ [see Figs. 6(c) and 6(d)]. Thus, the CMC model for $(n,m,u,v) = (1,1,3,-1)$ alone does not describe the range of the experimental data.

#### 3. Range of moiré periodicity and orientations for other indices

If we consider two additional sets of small indices, $(n,m,u,v) = (2,3,8,-4)$ and $(1,2,5,-3)$ [see arrows in Figs. 6(a) and 6(b) and simplified ball models in Fig. 6(e)], we generate a wider range of $\delta$ angles. For both of these sets of indices $\theta$ and $\lambda$ are in agreement with experiment [plots similar to Figs. 6(c) and 6(d); not shown], and $\delta$ is $57° \pm 2°$ and $61° \pm 2°$, respectively, also in agreement with the experimental data [see red and blue bars in Figs. 2(b) and 2(c)]. [As for $(n,m,u,v) = (1,1,3,-1)$, these results are obtained for $\alpha = 54.8°$; the corresponding unit cells are $0.442 \times 0.480$ and $0.445 \times 0.483$ nm$^2$ for $(n,m,u,v) = (2,3,8,-4)$ and $(1,2,5,-3)$, respectively]. In principle, one can consider many

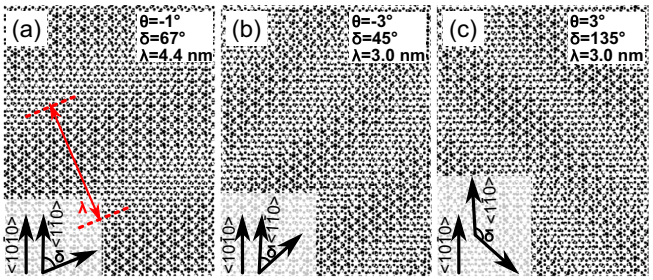


FIG. 8. (Color online) Simple superposition model: ball models for Bi unit cell 0.44 × 0.48 nm$^2$ (star symbols in Fig. 9) and three different misorientation angles $\theta$, (a) −1, (b) −3, and (c) +3°. In all images parts of atoms that overlap with the atoms in the graphite substrate are colored white (other atoms are black). $\delta$, $\lambda$, and the main crystallographic directions for the substrate and overlayer are indicated.

other sets of indices, but the three low-index sets discussed above reproduce the range of experimental values of $\lambda$ and $\delta$ quite well.

#### *4. CMC Summary*

The three low-index solutions of the CMC model highlighted above provide an adequate explanation of the experimental data. However, the CMC model allows only estimates of $\lambda$ by manual inspection of plots similar to Fig. 7(a) for each set of indices of interest, and for each value of $\alpha$ the corresponding value of $a_{rh}$ must then be calculated and compared with the range of experimentally measured unit cell dimensions. Hence, a detailed examination of all possible solutions of Eqs. (5)–(7) for all possible $\alpha$ is not practically possible. Therefore, we turn to a simpler alternative model of the moiré pattern in the next section.

### B. Qualitative model: Simple superposition

We now analyze a simple superposition model [23,67–70] that is analogous to the usual optical model of the interference pattern between two meshes [71]. First, we select a unit cell dimension to create a Bi slab. Next, the slab is overlaid on graphene, and we change the misorientation angle $\theta$. Figure 8 shows ball models generated for $A \times B = 0.44 \times 0.48$ nm$^2$ and $\theta = -1°$, $-3°$, and $3°$. We can then manually measure both $\delta$ and $\lambda$ as a function of $\theta$ for the selected unit cell dimension (see Fig. 8). The procedure is repeated for different Bi unit cell dimensions in order to find the best match between simulations and experimental results.

In our simulations we recognize the existence of two symmetries. The first is the substrate's threefold symmetry, which results in the same pattern every 60°. The other is related to the experimental difficulty of distinguishing the Bi[$\bar{1}$10] and Bi[1$\bar{1}$0] directions, which means that positive and negative rotations of the Bi slab [compare Figs. 8(b) and 8(c)] are effectively equivalent.

The dependence of $\delta$ and $\lambda$ on $\theta$ is shown in Fig. 9 for a range of realistic unit cell dimensions. Moiré patterns are observed for two $\theta$ ranges: −7° to 7° and 24° to 36°. The bottom plot shows that $\delta$ depends only weakly on the surface unit cell selection and that we can obtain the experimentally

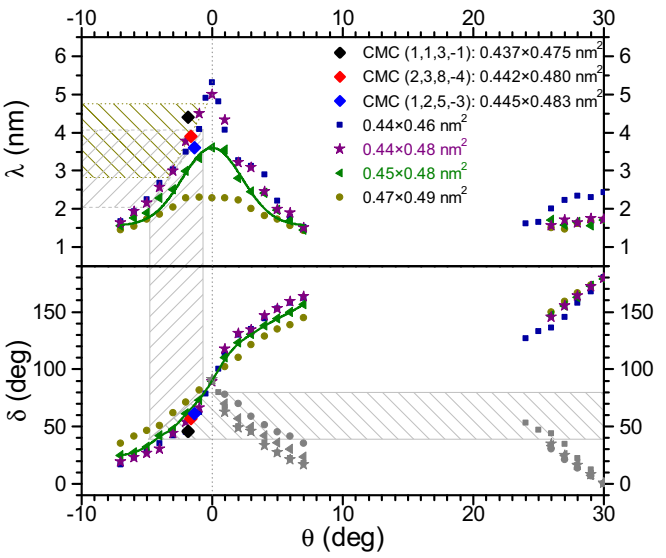


FIG. 9. (Color online) Simple superposition model: simulations of Bi slab rotation above graphene substrate showing the dependence of $\delta$ (bottom panel) and $\lambda$ (top panel) on $\theta$ and unit cell selection. Gray symbols are obtained with the symmetry transformation $180 - \delta \rightarrow \delta$ (see text). Crosshatched regions highlight the experimentally relevant range of values. The 0.45 × 0.48 nm$^2$ unit cell (green triangles and solid line) is similar to the bulk (0.454 × 0.475 nm$^2$). Data from the CMC model ($\alpha = 54.8°$; see Fig. 6) are shown (diamonds) to allow comparison of the results of the two models.

observed range of $\delta$ [∼ 40°–80°; see Fig. 2(b)] if $\theta$ is limited to the range ∼ −5° to ∼ −0.5° (gray crosshatched region in Fig. 9), which is in agreement with our STM and HR-TEM estimates ($\theta < 5°$). Due to the ambiguity between Bi[$\bar{1}$10] and Bi[1$\bar{1}$0] referred to in the previous paragraph, positive values of $\delta$ are transformed ($180 - \delta \rightarrow \delta$), making the data roughly symmetrical about the axis $\theta = 0$ in Fig. 9 (bottom), consistent with the ball models in Fig. 8.

The moiré periodicity $\lambda$ shows a strong dependence on surface unit cell dimensions (top plot in Fig. 9). For example, a misorientation angle $\theta$ in the range (−5.0°, −0.5°) gives $\lambda$ in the range 2–4 nm for bulk Bi lattice parameters (0.45 × 0.48 nm$^2$, gray crosshatched region in the top plot), which does not completely span the experimentally observed $\lambda$ values [Fig. 2(c)]. Good agreement is achieved only for $A$ smaller than the bulk value; for example, for $A \times B = 0.44 \times 0.48$ nm$^2$ (purple stars in Fig. 9) we find $-3.5° < \theta < -0.5°$ and 2.8 nm $< \lambda <$ 4.8 nm (green crosshatched region in the top plot in Fig. 9), which is in excellent agreement with experiment [Fig. 2(c)].

In summary, we are able to reproduce the range of experimental values of $\delta$ and $\lambda$ by a simple superposition model, as long as the length of one side of the unit cell [$A$; see Fig. 1(a)] is reduced below the bulk value by about 3%. $\lambda$ is much less dependent on the choice of the other unit cell dimension ($B$). The moiré pattern is observed for a narrow range of misorientations of the Bi islands with respect to the substrate ⟨10$\bar{1}$0⟩ direction, as in the experiments. The main disadvantage of this model is that it does not allow for quantitative calculation of the moiré pattern. In particular it is

not possible to calculate the dimensions of the moiré pattern unit cell, and all key parameters describing the moiré pattern ($\lambda$, $\theta$, $\delta$) have to be manually measured from ball models like those in Fig. 8.

## V. DISCUSSION

The range of moiré patterns observed experimentally can be explained by rotation of the Bi overlayer with respect to the graphite substrate. Both the CMC and simple superposition models provide adequate descriptions of the experimental data, but neither model provides a complete analytical framework for calculation of the moiré pattern parameters $\lambda$,$\delta$,$\theta$. The results of the two models are, however, consistent: compare the diamonds (CMC model) and other symbols (qualitative model) in Fig. 9.

Both models require that the *average* dimensions of the Bi unit cell across the Bi overlayer are slightly distorted in comparison to the bulk, but the remaining issue of interest is the question of how the regions in which the Bi and graphite lattices are commensurate and incommensurate are actually observed as a pattern by the STM. This requires a consideration of *local* distortions in the Bi overlayer.

### A. Distortion at the interface

It is immediately clear that as a result of local geometry (with respect to the substrate) atoms in the overlayer will experience forces which could distort their positions away from their normal equilibrium positions. It is then expected that these distortions will modify the local electronic states; indeed, the observed dependence of the moiré pattern on bias voltage [Fig. 5(d)] is consistent with such a modification. We suggest that the corrugation recorded by the STM as a result of the moiré pattern is caused by modulation of the LDOS by subsurface distortions while the surface itself remains undistorted [see model in Fig. 10(a)]. This is a similar to the nonadiabatic interface model proposed by Altfeder *et al.* [62]

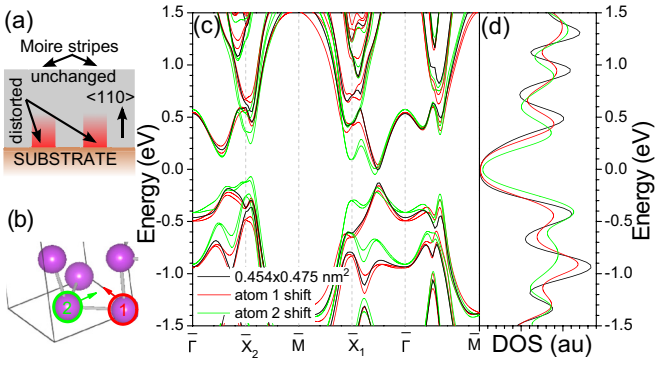


FIG. 10. (Color online) (a) Model showing moiré pattern formation as a result of distortion at the film-substrate interface (red shading). (b) Ball model of part of the unit cell showing the two atoms [1 (red) and 2 (blue)] that are shifted (along arrows) by 5% during DFT calculations. (c) DFT-calculated band diagrams for 2-ML-thick Bi films for a relaxed unit cell equal to $0.454 \times 0.475$ nm$^2$ (black) and distorted unit cells obtained by shifting atoms 1 (red) and 2 (blue) as indicated in (b). (d) Corresponding DOS.

which was used to explain the STM observation of the Si(111) $7 \times 7$ reconstruction on top of Pb islands. This model is further supported by DFT calculations described in the next section.

Before discussing the DFT calculations we emphasize that our STM results show that the moiré pattern forms only on 3-ML-thick islands and was never observed on thicker films (5, 7, . . . ML). This is strong evidence that the distortion occurs at the interface with the substrate, as in Refs. [62,63], and does not propagate all the way through the structure. This can be understood if one keeps in mind that the measured corrugation of the pattern is attenuated by a factor related to the film thickness: for example, in graphite it was shown (see Ref. [72] and references therein) that the attenuation factor (AF) can be expressed as $\mathrm{AF} = 2^n$, where $n$ corresponds to the number of graphite layers covering the misoriented one on which the superlattice is formed. If we apply this approach to Bi on HOPG, we can expect that the moiré pattern, if observed on a 5-ML-thick (7-ML-thick) island, would be 4 (16) times weaker than that observed on 3-ML-thick islands, and as a consequence would likely not be detectable at all.

### B. DFT calculations

Ideally, DFT calculations would be performed for Bi slabs in which the entire moiré unit cell is modeled; such calculations would require a huge number of atoms and would need to be performed for a huge number of orientations and lattice parameter values and so are not practically possible at present [30,51]. Instead, we note that the period of the moiré pattern is large compared to the atomic scale, so small distortions at the interface with the substrate will propagate relatively slowly in the plane of the Bi overlayer; this suggests that regions of high commensuration with the substrate can be modeled with a band structure obtained from the undistorted Bi unit cell, whereas the band structure for distorted unit cells corresponds to regions of low commensuration.

We start with a two-dimensional 2-ML-thick Bi film comprising a relaxed paired layer structure [30] and then introduce a distortion in the bottom layer and compare the obtained DOS. The distortion is introduced by a small shift (5%) of the atoms located in the bottom layer of the unit cell, while the surface atoms are kept in their original positions. The Bi unit cell contains two atoms in the bottom layer [see Fig. 10(b)]; thus, we perform calculations separately for displacement of atoms 1 and 2 [73].

Figures 10(c) and 10(d) show the calculated band dispersions and the DOS for the relaxed unit cell and the two distorted cases. As expected, the calculated DOS [Fig. 10(d)] differs only slightly for the three cases. The most important feature is that the DOS in the valley near the Fermi level increases for both distortions, but it is also observed that the location of the minimum and the intensity of the peaks change. We have obtained similar results for other distortions of the Bi unit cell (expansion and contraction of the unit cell both in lateral and vertical directions with respect to the paired layer plane; data not shown here). Hence, we conclude that any distortion of the positions of the atoms in the unit cell will result in modulation of the DOS. Thus, for a periodic distribution of regions in which the Bi lattice is under tension [as shown in Fig. 10(a)] one will obtain periodic modulation

of the LDOS. Hence, even for a morphologically featureless surface these LDOS modulations will affect the tunneling current, and the STM (operating in constant current mode) will measure height corrugations, leading to observation of the moiré pattern [5,74]. Distortions at the interface with the substrate will have smaller effects on the DOS of thicker films, which explains why the moiré pattern is observable in TEM images but not in STM images of structures with thicknesses $\geqslant 5$ ML.

Finally, we note that our analysis here might have important ramifications for the physics of ultrathin topological insulator films [28,29,31,32], which have attracted much recent interest because of their unusual properties. Such films are often grown on incommensurate substrates, where the interaction at the interface could lead to moiré pattern formation and structural modulation, as discussed here. In general, the coupling of electronic states at the two surfaces of an ultrathin topological insulator will usually result in a tunneling gap and hence in the loss of certain topological properties. An implication of our present study is that the distortion in the bottom layer can lead to splitting of the initially doubly degenerate bands [see Fig. 10(c); the black curve is doubly degenerate, whereas the red and blue curves are spin polarized]. Hence, we believe that the introduction of the tension at one of the surfaces (the interface with the substrate) could result in the reemergence of topologically protected states. Even a small distortion at the film-substrate interface could lead to spin texture of the surface states, which could be important for applications of topological insulators in nanotechnology and spintronics.

## VI. CONCLUSIONS

In conclusion, we have shown that Bi(110) films on HOPG exhibit a moiré pattern. In STM, the pattern is observed only in the ∼20% of 3-ML-thick islands (grains) which have the Bi$\langle\bar{1}10\rangle$ direction aligned close to the HOPG $\langle 10\bar{1}0\rangle$ (armchair) direction ($\theta < 5^\circ$). These islands also appear to have slightly different unit cells than those without a moiré pattern. These results are consistent with HR-TEM data that show moiré patterns in thicker films.

The pattern of commensurate and incommensurate regions at the film-substrate interface locally introduces tension in the film, which distorts atomic locations on one surface of the Bi film and results in the formation of a periodic modulation of the LDOS that is measured by the STM. This modulation could lead to the emergence of spin-textured topological states.

## ACKNOWLEDGMENTS

This work was supported by the MacDiarmid Institute for Advanced Materials and Nanotechnology (P.J.K., O.M., and S.A.B.) and the U.S. National Science Foundation (Grant No. DMR 13-05583, T.-C.C.).

## APPENDIX A: GRAIN BOUNDARIES

Since the moiré pattern observed above is connected strongly to the presence of grain boundaries between Bi crystallites, we briefly summarize our previous findings related to tilt grain boundaries. For further details the reader is referred to Ref. [37].

We describe the tilt grain boundary [see Fig. 1(a) for the ball model] using the periodicity vector $\vec{P}_N = N \cdot \vec{B} - \vec{A}$ along the boundary, where $N$ is a natural number. The unit cell is shown in Fig. 1(a) and is described in Sec. I A.

The determination of $N$ (valid only for odd values) allows one to calculate the boundary plane $\{hkl\}$ separating two grains:

$$\begin{aligned} h &= (c/a)^2(2-N) - 3(N+1), \\ k &= (c/a)^2(2+N) + 3(N-1), \\ l &= 2[3+(c/a)^2], \end{aligned} \tag{A1}$$

and also

$$\Sigma_N = \frac{|N \cdot \vec{B} - \vec{A}||\vec{B} + N \cdot \vec{A}|}{2AB}. \tag{A2}$$

Using the above formalism, the most common grain boundary ($N = 1$) can be classified as a $\Sigma 1\,[110]\,(1\,26\,25)$ (simply denoted $\Sigma 1$). In our previous experiments [37] we observed odd $N$'s up to $N = 21$ ($\Sigma 221\,[110]\,(\overline{10}\,11\,1)$).

Measurement of a dihedral angle $\varphi$ between two grains in a $\Sigma 1$ grain boundary [see Fig. 1(a)] can be used to estimate the ratio of the unit cell dimensions:

$$B/A = \tan(\varphi/2). \tag{A3}$$

Equation (A3) is very useful because one can make a first estimation of the surface unit cell based on the angle measured between two known directions in grains using only low-resolution STM or SEM images.

Finally, measurement of the angle between surface unit cell diagonals $\gamma$ and interplane distance $d$ [see Fig. 1(a)] also allows one to estimate surface unit-cell dimensions:

$$\begin{aligned} A &\simeq 2d\cos(\gamma/2), \\ B &\simeq 2d\sin(\gamma/2), \end{aligned} \tag{A4}$$

where $\gamma = \varphi$ for $N = 1$. We can apply this method to Fig. 3(a). If we assume $A^{\text{bulk}} = 0.454$ nm, then $B \sim 0.487$ nm ($B^{\text{bulk}} = 0.475$ nm is smaller by 3% since $\varphi^{\text{bulk}} = 92.6^\circ$); alternatively, if $A = 0.44$ nm, then $B \sim 0.48$ nm. The latter estimate is in very good agreement with direct measurement of the surface unit cell from the high-resolution STM image shown in Fig. 3(b).

## APPENDIX B: FFT ANALYSIS

In order to investigate modulation of the LDOS by the moiré pattern we apply a statistical approach. For each of the high-resolution CITS data sets recorded on moiré patterns (over 550 000 STS curves in 34 individual CITS experiments were recorded using different tips and on different samples) we calculated the FFT of $dI/dV$ spatial maps recorded in the range of ±1 eV around the Fermi level. One such FFT is shown in Fig. 5(c). Clear spots in these FFT images [indicated by a circle in Fig. 5(c)] correspond to modulation of the $dI/dV$ data by the moiré pattern. Next, for each data set we created a plot of the moiré spot intensity (after background subtraction)

as a function of energy. Such plots were normalized to the range [0; 1] and averaged (across all CITS experiments), and the final plot was again normalized to [0; 1] [see plot 3 in Fig. 5(e)]. The most pronounced feature, in the range of −0.1 to +0.2 V [denoted M in Fig. 5(d)], corresponds to modulation of the LDOS valley (near zero bias), and there is a weaker peak near −0.3 V, close to the position of the first peak in the DOS below the Fermi level [gray band in Fig. 5(d)].


[1] A. D. Novaco and J. P. McTague, Phys. Rev. Lett. **38**, 1286 (1977).
[2] J. P. McTague and A. D. Novaco, Phys. Rev. B **19**, 5299 (1979).
[3] J. M. Martin, C. Donnet, T. Le Mogne, and T. Epicier, Phys. Rev. B **48**, 10583 (1993).
[4] G. Ye, M. A. Crimp, and J. Nogami, Phys. Rev. B **74**, 033104 (2006).
[5] K. Kobayashi, Phys. Rev. B **53**, 11091 (1996).
[6] K. Kobayashi, Phys. Rev. B **50**, 4749 (1994).
[7] G. Ketteler and W. Ranke, Phys. Rev. B **66**, 033405 (2002).
[8] M. Hupalo, V. Yeh, T. L. Chan, C. Z. Wang, K. M. Ho, and M. C. Tringides, Phys. Rev. B **71**, 193408 (2005).
[9] S. M. Lu, M. C. Yang, W. B. Su, C. L. Jiang, T. Hsu, C. S. Chang, and T. T. Tsong, Phys. Rev. B **75**, 113402 (2007).
[10] M. Pivetta, F. Patthey, M. Stengel, A. Baldereschi, and W.-D. Schneider, Phys. Rev. B **72**, 115404 (2005).
[11] E. D. L. Rienks, N. Nilius, H.-P. Rust, and H.-J. Freund, Phys. Rev. B **71**, 241404 (2005).
[12] E. D. L. Rienks, N. Nilius, L. Giordano, J. Goniakowski, G. Pacchioni, M. P. Felicissimo, T. Risse, H.-P. Rust, and H.-J. Freund, Phys. Rev. B **75**, 205443 (2007).
[13] T. R. Albrecht, H. A. Mizes, J. Nogami, S.-i. Park, and C. F. Quate, Appl. Phys. Lett. **52**, 362 (1988).
[14] B. Nysten, J.-C. Roux, S. Flandrois, C. Daulan, and H. Saadaoui, Phys. Rev. B **48**, 12527 (1993).
[15] J. C. Patrin, Y. Z. Li, M. Chander, and J. H. Weaver, Phys. Rev. B **46**, 10221 (1992).
[16] U. Müller, D. Carnal, H. Siegenthaler, E. Schmidt, W. J. Lorenz, W. Obretenov, U. Schmidt, G. Staikov, and E. Budevski, Phys. Rev. B **46**, 12899 (1992).
[17] Z. Y. Rong and P. Kuiper, Phys. Rev. B **48**, 17427 (1993).
[18] M. Kuwabara, D. R. Clarke, and D. A. Smith, Appl. Phys. Lett. **56**, 2396 (1990).
[19] R. Pushpa and S. Narasimhan, Phys. Rev. B **67**, 205418 (2003).
[20] J. Repp, G. Meyer, and K.-H. Rieder, Phys. Rev. Lett. **92**, 036803 (2004).
[21] Y. Pan, M. Gao, L. Huang, F. Liu, and H.-J. Gao, Appl. Phys. Lett. **95**, 093106 (2009).
[22] N. Nilius, E. D. L. Rienks, H.-P. Rust, and H.-J. Freund, Phys. Rev. Lett. **95**, 066101 (2005).
[23] N. Fukui, Y. Suwa, H. Yoshida, T. Sugai, S. Heike, M. Fujimori, Y. Terada, T. Hashizume, and H. Shinohara, Phys. Rev. B **79**, 125402 (2009).
[24] H. Y. Lin, Y. P. Chiu, L. W. Huang, Y. W. Chen, T. Y. Fu, C. S. Chang, and T. T. Tsong, Phys. Rev. Lett. **94**, 136101 (2005).
[25] S. Marchini, S. Günther, and J. Wintterlin, Phys. Rev. B **76**, 075429 (2007).
[26] Y. Wang, Y. Ye, and K. Wu, Surf. Sci. **600**, 729 (2006).
[27] Z. Sun, S. K. Hämäläinen, J. Sainio, J. Lahtinen, D. Vanmaekelbergh, and P. Liljeroth, Phys. Rev. B **83**, 081415 (2011).
[28] J. E. Moore, Nature (London) **464**, 194 (2010).
[29] X.-L. Qi and S.-C. Zhang, Rev. Mod. Phys. **83**, 1057 (2011).
[30] P. J. Kowalczyk, O. Mahapatra, S. A. Brown, G. Bian, X. Wang, and T.-C. Chiang, Nano Lett. **13**, 43 (2013).
[31] D. Hsieh, D. Qian, L. Wray, Y. Xia, Y. Hor, R. Cava, and M. Hasan, Nature **452**, 970 (2008).
[32] X. G. Zhu and P. Hofmann, Phys. Rev. B **89**, 125402 (2014).
[33] C. H. Chen, K. D. Kepler, A. A. Gewirth, B. M. Ocko, and J. Wang, J. Phys. Chem. **97**, 7290 (1993).
[34] S. Yaginuma, T. Nagao, J. Sadowski, M. Saito, K. Nagaoka, Y. Fujikawa, T. Sakurai, and T. Nakayama, Surf. Sci. **601**, 3593 (2007).
[35] S. Bobaru, E. Gaudry, M.-C. de Weerd, J. Ledieu, and V. Fournée, Phys. Rev. B **86**, 214201 (2012).
[36] S. Scott, M. Kral, and S. Brown, Surf. Sci. **587**, 175 (2005).
[37] P. Kowalczyk, D. Belić, O. Mahapatra, and S. Brown, Acta Mater. **60**, 674 (2012).
[38] A. Tkatchenko, Phys. Rev. B **75**, 235411 (2007).
[39] P. Hofmann, Prog. Surf. Sci. **81**, 191 (2006).
[40] A. Stróżecka, A. Eiguren, and J. I. Pascual, Phys. Rev. Lett. **107**, 186805 (2011).
[41] A. Takayama, T. Sato, S. Souma, T. Oguchi, and T. Takahashi, Nano Lett. **12**, 1776 (2012).
[42] I. Žotić, J. Fabian, and S. Das Sarma, Rev. Mod. Phys. **76**, 323 (2004).
[43] C. R. Ast and H. Höchst, Phys. Rev. Lett. **87**, 177602 (2001).
[44] Y. Liu and R. E. Allen, Phys. Rev. B **52**, 1566 (1995).
[45] M. E. T. Molares, N. Chtanko, T. W. Cornelius, D. Dobrev, I. Enculescu, R. H. Blick, and R. Neumann, Nanotechnology **15**, S201 (2004).
[46] T. Hirahara, T. Nagao, I. Matsuda, G. Bihlmayer, E. V. Chulkov, Y. M. Koroteev, and S. Hasegawa, Phys. Rev. B **75**, 035422 (2007).
[47] B. Weitzel and H. Micklitz, Phys. Rev. Lett. **66**, 385 (1991).
[48] V. De Renzi, M. G. Betti, and C. Mariani, Phys. Rev. B **48**, 4767 (1993).
[49] C. A. Hoffman, J. R. Meyer, F. J. Bartoli, A. Di Venere, X. J. Yi, C. L. Hou, H. C. Wang, J. B. Ketterson, and G. K. Wong, Phys. Rev. B **48**, 11431 (1993).
[50] Y.-M. Lin, X. Sun, and M. S. Dresselhaus, Phys. Rev. B **62**, 4610 (2000).
[51] M. Wada, S. Murakami, F. Freimuth, and G. Bihlmayer, Phys. Rev. B **83**, 121310 (2011).
[52] T. Hirahara, G. Bihlmayer, Y. Sakamoto, M. Yamada, H. Miyazaki, S.-i. Kimura, S. Blügel, and S. Hasegawa, Phys. Rev. Lett. **107**, 166801 (2011).
[53] S. A. Scott, M. V. Kral, and S. A. Brown, Phys. Rev. B **72**, 205423 (2005).
[54] S. A. Scott, M. V. Kral, and S. A. Brown, Phys. Rev. B **73**, 205424 (2006).
[55] D. N. McCarthy, D. Robertson, P. J. Kowalczyk, and S. A. Brown, Surf. Sci. **604**, 1273 (2010).
[56] P. Kowalczyk, O. Mahapatra, D. McCarthy, W. Kozlowski, Z. Klusek, and S. Brown, Surf. Sci. **605**, 659 (2011).

[57] P. J. Kowalczyk, D. Belic, O. Mahapatra, S. A. Brown, E. S. Kadantsev, T. K. Woo, B. Ingham, and W. Kozlowski, Appl. Phys. Lett. **100**, 151904 (2012).
[58] H. L. Zhang, W. Chen, X. S. Wang, J. Yuhara, and A. T. S. Wee, Appl. Surf. Sci. **256**, 460 (2009).
[59] T. Nagao, J. T. Sadowski, M. Saito, S. Yaginuma, Y. Fujikawa, T. Kogure, T. Ohno, Y. Hasegawa, S. Hasegawa, and T. Sakurai, Phys. Rev. Lett. **93**, 105501 (2004).
[60] H. R. Sharma, V. Fournée, M. Shimoda, A. R. Ross, T. A. Lograsso, P. Gille, and A. P. Tsai, Phys. Rev. B **78**, 155416 (2008).
[61] F. J. Giessibl, Rev. Mod. Phys. **75**, 949 (2003).
[62] I. B. Altfeder, V. Narayanamurti, and D. M. Chen, Phys. Rev. Lett. **88**, 206801 (2002).
[63] M. Yakes and M. Tringides, J. Phys. Chem. A **115**, 7096 (2011).
[64] G. Bian, T. Miller, and T.-C. Chiang, Phys. Rev. B **80**, 245407 (2009).
[65] Y. M. Koroteev, G. Bihlmayer, E. V. Chulkov, and S. Blügel, Phys. Rev. B **77**, 045428 (2008).
[66] H. I. Li, K. J. Franke, J. I. Pascual, L. W. Bruch, and R. D. Diehl, Phys. Rev. B **80**, 085415 (2009).
[67] H. Li, H. Peng, W. Dang, L. Yu, and Z. Liu, Front. Phys. **7**, 208 (2012).
[68] J. Cho, L. Gao, J. Tian, H. Cao, W. Wu, Q. Yu, E. N. Yitamben, B. Fisher, J. R. Guest, Y. P. Chen *et al.*, ACS Nano **5**, 3607 (2011).
[69] C.-L. Song, Y.-L. Wang, Y.-P. Jiang, Y. Zhang, C.-Z. Chang, L. Wang, K. He, X. Chen, J.-F. Jia, Y. Wang *et al.*, Appl. Phys. Lett. **97**, 143118 (2010).
[70] J. M. Campanera, G. Savini, I. Suarez-Martinez, and M. I. Heggie, Phys. Rev. B **75**, 235449 (2007).
[71] I. Amidror, *The Theory of the Moiré Phenomenon*, Computational Imaging and Vision (Kluwer Academic, London, 2000).
[72] W.-T. Pong and C. Durkan, J. Phys. D **38**, R329 (2005).
[73] Note that the experimentally observed wetting layer does not contribute to the electronic structure of the film [30], so it is ignored in these calculations. The exact nature of the wetting layer is still unclear.
[74] K. Kobayashi and J. Yamauchi, Phys. Rev. B **51**, 17085 (1995).